

Dynamic Modelling, Control, and Stability Analysis of DC Modular Multilevel Converter Connected to HVDC Cables

Salman Badkubi, *Student Member, IEEE*, Aliakbar Jamshidi Far, *Member, IEEE*,
and Sumeet S. Aphale, *Senior Member, IEEE*

Abstract—Innovative dynamic models for the DC modular multilevel converter (DC-MMC) in rotating dq frame are presented in this paper, which are specifically designed to enhance converter design and stability analysis. Open-loop and closed-loop models are developed using three dq frames, providing a detailed examination of the impact of 2nd and 3rd harmonic components on the model accuracy. A novel contribution of this paper is the integration of a 2nd harmonic current suppression controller (SHCSC) within the closed-loop model, offering new insights into its effects on system stability. The DC-MMC model is further extended by coupling it with high-voltage direct current (HVDC) cables on each side, forming an interconnected system model that accurately represents a more authentic scenario for future DC grids. The proposed model is rigorously validated against PSCAD benchmark model, confirming their precision and reliability. The interconnected system model is then utilized to analyze the influence of cable length on system stability, demonstrating practical applications. The closed-loop model is subsequently employed for stability assessment of the interconnected system, showcasing its applicability in real-world scenarios. Additionally, a damping controller is designed using participation factor and residue approaches, offering a refined approach to oscillation damping and stability optimization. The effectiveness of the controller is evaluated through eigenvalue analysis, supported by simulation results, underscoring its potential for enhancing system stability.

Index Terms—High-voltage direct current, dynamic modeling, modular multilevel converter, stability, eigenvalue analysis, damping controller.

I. INTRODUCTION

DC/DC converters are poised to play a crucial role in the development of multi-terminal high-voltage direct current (HVDC) and DC grids. These converters facilitate key functionalities such as enabling power trading between DC systems with varying or equal voltage levels, ensuring in-

teroperability, supporting bidirectional power flow control, and providing stabilization and DC fault isolation capabilities [1]-[5]. CIGRE has recognized the importance of DC/DC converters, exploring their applications through various working groups, including WG B4.52 on the feasibility of DC grids [6], WG B4.58 on power flow controllers in meshed HVDC grids [7], and WG B4.76 on DC/DC converter applications in HVDC and DC grids [8].

There are two primary families of HVDC DC/DC converters: isolated converters, typically employing the dual active bridge topology with a two-stage DC/AC/DC conversion process; and non-isolated converters based on modular multilevel converter (MMC) technology, referred to as DC modular multilevel converters (DC-MMCs), which utilizes a single-stage conversion approach.

DC-MMCs are emerging as a potential cost-effective solution for interconnecting HVDC systems, particularly due to their lower capital costs and reduced power losses compared with isolated DC/DC converters, resulting from the elimination of the additional conversion step. This advantage is especially significant when the DC voltage step ratio is low, and the HVDC systems share similar configurations. Most HVDC systems operate at a few hundred kilovolts, leading to a low DC voltage step ratio in HVDC-HVDC interconnections. This low ratio ensures high component utilization within the DC-MMC. Furthermore, since the majority of current and planned HVDC systems are configured as monopole symmetrical or bipole voltage source converter based HVDC (VSC-HVDC) links, the DC-MMC presents itself as a highly suitable option for interconnecting these HVDC systems.

The concept, design, and control principles of DC-MMC have been discussed extensively in [1]-[3], with comparisons to isolated dual active bridge DC/DC converters for HVDC and medium-voltage DC (MVDC) applications provided in [9]. A phasor-domain steady-state model for DC-MMC is introduced in [10], which serves as the foundation for subsequent converter and control design in [11]. However, this model only accounts for DC and fundamental frequency components, overlooking the 2nd harmonic components and their interaction with other coordinate frames, thus reducing the model accuracy. Similar oversimplifications are found in the linearized model presented in [12]. Although a more detailed analytical phasor model is provided in [13], it remains

Manuscript received: December 19, 2023; revised: May 12, 2024; accepted: September 18, 2024. Date of CrossCheck: September 18, 2024. Date of online publication: October 15, 2024.

This work was partially supported by Petrofac through the Petrofac Ph. D. Scholarship.

This article is distributed under the terms of the Creative Commons Attribution 4.0 International License (<http://creativecommons.org/licenses/by/4.0/>).

S. Badkubi (corresponding author), A. J. Far, and S. S. Aphale are with the School of Engineering, University of Aberdeen, Aberdeen, UK (e-mail: s.badkubi.21@abdn.ac.uk; ajamshidifar@abdn.ac.uk; s.aphale@abdn.ac.uk).

DOI: 10.35833/MPCE.2023.001004



focused on the steady-state analysis of converter currents, voltages, and power flow, neglecting the dynamic behavior of the converter. These oversights highlight the need for more comprehensive models that incorporate dynamic factors to improve the accuracy and reliability of DC-MMC in future DC grid applications.

A significant gap in the existing literature is the assumption that DC-MMCs are connected to rigid DC sources on both ends. This simplification ignores the dynamic interactions between the DC-MMC and other interconnected DC subsystems, which is crucial for understanding the stability and control of future DC grids. In the anticipated future configuration of DC grids, each side of a DC-MMC will be connected to other DC systems through HVDC cables or lines. These interconnections introduce additional complexities that have not been fully addressed in previous research [14]. The dynamic interactions among multiple DC systems, mediated by HVDC cables, could significantly influence the overall stability and control of the DC grid, necessitating a more thorough investigation into these aspects.

This paper seeks to address these knowledge gaps by investigating the impact of the 2nd and higher harmonics on the accuracy of the DC-MMC model. This paper reveals the critical importance of the 2nd harmonic in the model, while demonstrating that higher harmonics have a negligible impact and can be safely ignored.

The proposed model is then applied to evaluate the influence of HVDC cables connected to both sides of the DC-MMC on its control and stability. HVDC cables are meticulously modeled using cascaded proportional-integral (PI) sections with parallel RL branches [15], [16]. The parameters of the parallel RL branches are estimated via the vector-fitting approach [17]. The study shows that long HVDC cables introduce oscillations and potential instability into the interconnected system, which is analyzed using eigenvalue analysis techniques [18]. The proposed model is further employed to design a damping controller to suppress these oscillations and stabilize the system, utilizing participation factor (PF) and residue approaches [19], [20]. Notably, the study identifies the 2nd harmonic component of the upper-arm sum voltage as the most effective feedback signal, underscoring the significance of the 2nd harmonic components in the modeling and control of DC-MMC. The key contributions of this paper can be summarized as follows.

1) Accurate dynamic phasor model: this paper introduces a novel closed-loop dynamic phasor model for DC-MMC, incorporating the 2nd harmonic dynamics and evaluating the impact of higher harmonics on model accuracy. Additionally, the dynamics of the 2nd harmonic current suppression controller (SHCSC) is modeled and integrated into the closed-loop DC-MMC model.

2) Realistic test case: this paper presents a realistic test case where DC-MMC is connected to HVDC cables on both sides, allowing for an in-depth analysis of DC voltage dynamics and the effects on the stability and control of the DC-MMC and broader interconnected system.

3) Application example and controller design: the proposed model is used to examine the impact of HVDC cables

of varying lengths on system performance and stability, followed by the design of a damping controller to mitigate oscillations.

This comprehensive approach aims to enhance the understanding of DC-MMC performance, positioning it as a potentially cost-effective single-stage DC/DC converter for future DC grid applications, particularly in the interconnection of HVDC links and systems.

II. DC-MMC

A. Converter Structure

Figure 1 illustrates the structure of a unipolar p -phase DC-MMC [3], where V_1 and V_2 are the high voltage (HV) and low voltage (LV) side voltages of DC-MMC, respectively; I_1 and I_2 are the HV and LV side DC currents of DC-MMC, respectively; i_{armU} and i_{armL} are the upper- and lower-arm currents, respectively; V_U^Σ and V_L^Σ are the upper- and lower- arm sum voltages, respectively; R_{armU} and R_{armL} are the upper- and lower-arm equivalent resistances, respectively; C_{smU} and C_{smL} are the upper and lower submodule capacitances, respectively; L_{armU} and L_{armL} are the upper- and lower-arm inductances, respectively; V_{armU} and V_{armL} are the upper- and lower-arm voltages, respectively; and L_2 is the line inductance. In each lower arm, there are N_L half-bridge submodules (HBSMs). The upper arms consist of full-bridge submodules (FBSMs) to provide fault-blocking capabilities [2]. It is worth mentioning that the fault-blocking capability can be achieved by incorporating a specific number of submodules only in the upper arm, denoted as $N_{U,FBSM}$. This reduces the capital cost and power losses while maintaining fault isolation between the two sides of the DC-MMC by generating voltage $-V_2$ in the upper arm to prevent the HV fault propagation to the LV side [21]. However, for simplicity, all the submodules in the upper arm in Fig. 1 are shown as FBSMs.

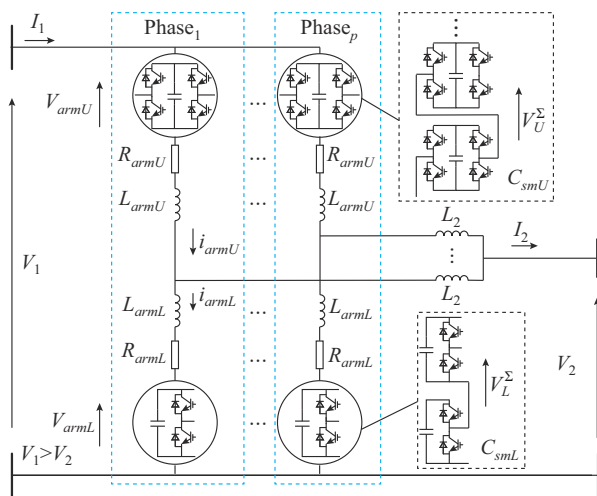


Fig. 1. Structure of a unipolar p -phase DC-MMC.

B. Dynamic Equations of DC-MMC

The dynamic equations of the DC-MMC are given in [3], and a summary is included here for completeness. The constituent dynamic equations for arm currents and arm sum

voltages are:

$$\frac{d}{dt} \begin{bmatrix} i_{armU} \\ i_{armL} \end{bmatrix} = \frac{-1}{L_Z} \begin{bmatrix} R_{armU} L_{2L} & R_{armL} L_2 \\ R_{armU} L_{2U} & R_{armL} L_{2U} \end{bmatrix} \begin{bmatrix} i_{armU} \\ i_{armL} \end{bmatrix} - \frac{1}{L_Z} \begin{bmatrix} L_{2L} & L_2 \\ L_2 & L_{2U} \end{bmatrix} \begin{bmatrix} m_U v_U^\Sigma \\ m_L v_L^\Sigma \end{bmatrix} + \frac{1}{L_Z} \begin{bmatrix} L_{2L} & -L_{armL} \\ L_2 & L_{armU} \end{bmatrix} \begin{bmatrix} V_1 \\ V_2 \end{bmatrix} \quad (1)$$

$$\frac{d}{dt} \begin{bmatrix} v_U^\Sigma \\ v_L^\Sigma \end{bmatrix} = \begin{bmatrix} 0 & 0 \\ 0 & 0 \end{bmatrix} \begin{bmatrix} v_U^\Sigma \\ v_L^\Sigma \end{bmatrix} + \begin{bmatrix} \frac{1}{C_{armU}} m_U i_{armU} \\ \frac{1}{C_{armL}} m_L i_{armL} \end{bmatrix} \quad (2)$$

$$\begin{cases} L_Z = L_{armU} L_{armL} + L_{armU} L_2 + L_{armL} L_2 \\ L_{2L} = L_2 + L_{armL} \\ L_{2U} = L_2 + L_{armU} \\ C_{armU} = \frac{C_{smU}}{N_U} \\ C_{armL} = \frac{C_{smL}}{N_L} \end{cases} \quad (3)$$

where m_U and m_L are the upper- and lower-arm control signals, respectively; and C_{armU} and C_{armL} are the upper- and lower-arm submodule capacitances, respectively.

III. DYNAMIC OPEN-LOOP dq MODEL

A. Assumptions and Definitions

The assumptions are made as follows.

1) The DC-MMC operates in the balanced mode, where all phases exhibit uniformity, characterized by the same DC component and sinusoidal AC components with a 120° phase shift in the case of a three-phase DC-MMC.

2) The upper- and lower-arm currents for one phase-leg are composed of DC, fundamental frequency, and higher harmonics components given by:

$$\begin{cases} i_{armU}(t) = I_{U0} + \sum_{i=1}^n I_{Ui} \cos(\omega_i t + \theta_{Ui}) = I_{U0} + \sum_{i=1}^n I_{Udi} \cos(\omega_i t) + \sum_{i=1}^n I_{Uqi} \sin(\omega_i t) \\ i_{armL}(t) = I_{L0} + \sum_{i=1}^n I_{Li} \cos(\omega_i t + \theta_{Li}) = I_{L0} + \sum_{i=1}^n I_{Ldi} \cos(\omega_i t) + \sum_{i=1}^n I_{Lqi} \sin(\omega_i t) \end{cases} \quad (4)$$

where the subscripts $U0$ and $L0$ denote the DC components of the upper and lower arms, respectively; the subscripts Ui and Li denote the i^{th} harmonic amplitudes of the upper- and lower-arm currents, respectively; $\omega_i = 2\pi fi$, and f is the arbitrarily selected internal operating frequency of the DC-MMC; θ_{Ui} and θ_{Li} are the phase shifts of the upper- and lower-arm currents, respectively; and the subscripts Udi , Uqi and Ldi , Lqi denote the i^{th} harmonic dq components of upper- and lower-arm currents, respectively. At the outset, we assume that the arm currents encompass all harmonics. However, it will be demonstrated later in this paper that harmonics of order 3 and above exert negligible influence on the

model accuracy and can thus be disregarded. The arm currents of the other phase-legs can be analogously represented, incorporating a phase shift of $360/p$, where p denotes the number of phases.

3) Similarly, the upper- and lower-arm sum voltages for one phase-leg can be represented as:

$$\begin{cases} v_U^\Sigma(t) = V_{U0}^\Sigma + \sum_{i=1}^n V_{Ui}^\Sigma \cos(\omega_i t + \theta_{vUi}) = V_{U0}^\Sigma + \sum_{i=1}^n V_{Udi}^\Sigma \cos(\omega_i t) + \sum_{i=1}^n V_{Uqi}^\Sigma \sin(\omega_i t) \\ v_L^\Sigma(t) = V_{L0}^\Sigma + \sum_{i=1}^n V_{Li}^\Sigma \cos(\omega_i t + \theta_{vLi}) = V_{L0}^\Sigma + \sum_{i=1}^n V_{Ldi}^\Sigma \cos(\omega_i t) + \sum_{i=1}^n V_{Lqi}^\Sigma \sin(\omega_i t) \end{cases} \quad (5)$$

where θ_{vUi} and θ_{vLi} are the phase shifts of the upper- and lower-arm voltages, respectively.

4) The control signals may or may not include a 2^{nd} harmonic component, depending on whether the control incorporates SHCSC. Initially, this paper addresses control without SHCSC, followed by its addition. Consequently, at this stage, the control signals for both upper and lower arms are considered to contain only DC and fundamental components [11]:

$$\begin{cases} m_U(t) = M_{U0} + M_U \cos(\omega t) \\ m_L(t) = M_{L0} + M_L \cos(\omega t + \theta_{mL}) = M_{L0} + M_{Ld} \cos(\omega t) + M_{Lq} \sin(\omega t) \end{cases} \quad (6)$$

It is worth noting that the upper control signal has only M_{U0} and M_{Ud} components ($M_{Ud} = M_U$), and the lower control signal has only M_{L0} , M_{Ld} , and M_{Lq} components.

B. 2^{nd} -order Open-loop dq Model

The dynamic equations for the DC component, fundamental frequency, and 2^{nd} harmonics of the DC-MMC are formulated in [22]. These equations can be expressed as a 2^{nd} -order open-loop dq model for the DC-MMC in the matrix form as:

$$\dot{\mathbf{x}}_{OL2} = \mathbf{f}_{OL2}(\mathbf{x}_{OL2}, \mathbf{u}_{OL}) \quad (7)$$

where \mathbf{x}_{OL2} , \mathbf{u}_{OL} , and \mathbf{f}_{OL2} are defined in Supplementary Material A.

C. 3^{rd} and Higher Harmonics

The 3^{rd} and higher harmonics can be modelled in a similar way to the 2^{nd} harmonic [22]. However, as it is investigated in this paper, the 3^{rd} and higher harmonics have negligible impact on the model accuracy, and therefore they have not been presented here for space brevity.

IV. DYNAMIC CLOSED-LOOP dq MODEL

A. Controller Model

There are various options available for the DC-MMC controller, and Fig. 2 illustrates a DC-MMC control block [13], as considered in [2], where the subscript ref represents the reference value. This controller incorporates five PI control loops (k_{pj}, k_{ij}), $j = 1, 2, \dots, 5$. Specifically, the control signals

M_{U0} and M_{L0} are responsible for ensuring energy balancing in the converter arms by regulating the arm sum voltages. The inner current control loops play a crucial role in improving the system response and restricting the upper- and lower-arm currents under abnormal operating conditions. The phase shift ϕ_{mL} of the lower-arm fundamental component is employed to regulate the DC power flow P_{dc} towards the reference value $P_{dc,ref}$. Typically, the reference values for the arm sum voltages V_{U0ref}^Σ and V_{L0ref}^Σ are chosen to be constant and equal to the rated voltage of the HV side, i.e., V_1^{rated} [13].

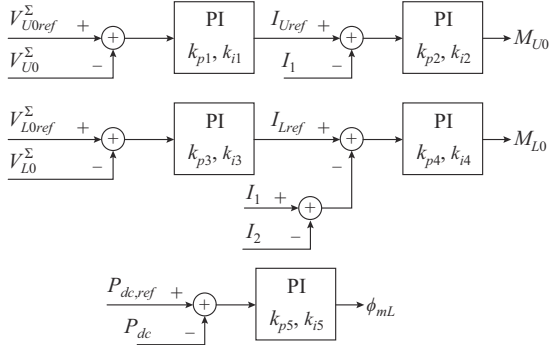


Fig. 2. DC-MMC control block.

The controller, in conjunction with the following equation, generates the control signals $m_U(t)$ and $m_L(t)$ as expressed in (6), or equivalently the five control signals M_{U0} , M_{L0} , M_U , M_{Ld} , and M_{Lq} in dq frame [13]:

$$\begin{cases} M_U = M_L = \min(M_{U0}, M_{L0}) \\ M_{Ld} = M_L \cos \phi_{mL} \\ M_{Lq} = M_L \sin \phi_{mL} \end{cases} \quad (8)$$

The controller dynamic equations can be derived from the control block as:

$$\frac{d}{dt} \underbrace{\begin{bmatrix} I_{Uref} \\ M_{U0} \\ I_{Lref} \\ M_{L0} \\ \phi_{mL} \end{bmatrix}}_{\mathbf{x}_{ctrl}} = \underbrace{\begin{bmatrix} -k_{p1} \frac{d}{dt} V_{U0}^\Sigma + k_{i1} (V_{U0ref}^\Sigma - V_{U0}^\Sigma) \\ k_{p2} \left(\frac{d}{dt} I_{Uref} - 3 \frac{d}{dt} I_{U0} \right) + k_{i2} (I_{Uref} - 3I_{U0}) \\ -k_{p3} \frac{d}{dt} V_{L0}^\Sigma + k_{i3} (V_{L0ref}^\Sigma - V_{L0}^\Sigma) \\ k_{p4} \left(\frac{d}{dt} I_{Lref} - 3 \frac{d}{dt} I_{L0} \right) + k_{i4} (I_{Lref} - 3I_{L0}) \\ -k_{p5} V_1 \left(3 \frac{d}{dt} I_{U0} \right) + k_{i5} (P_{dc,ref} - 3V_1 I_{U0}) \end{bmatrix}}_{\mathbf{f}_{ctrl}(\mathbf{x}_{OL2}, \mathbf{u}_{CL})} \quad (9)$$

where $k_{p1} = k_{p3}$; $k_{i1} = k_{i3}$; $k_{p2} = k_{p4}$; and $k_{i2} = k_{i4}$.

B. SHCSC

While the 2nd harmonic arm currents in DC-MMC are typically lower compared with those in conventional AC/DC MMC, a similar SHCSC can be implemented to mitigate them [23]. Each of the four variables associated with the 2nd harmonic arm currents (I_{Ud2} , I_{Ld2} , I_{Uq2} , and I_{Lq2}) requires an individual PI control loop. Consequently, the implementation of SHCSC necessitates the use of four PI loops.

The control signals (6) for the DC-MMC with SHCSC are

then modified as:

$$\begin{cases} m_U(t) = M_{U0} + M_U \cos(\omega t) + M_{U2} \cos(2\omega t + \theta_{mU2}) \\ m_L(t) = M_{L0} + M_L \cos(\omega t + \theta_{mL}) + M_{L2} \cos(2\omega t + \theta_{mL2}) \end{cases} \quad (10)$$

This modification means that the 2nd harmonic dq components M_{Ud2}/M_{Uq2} and M_{Ld2}/M_{Lq2} are added to the control signals in dq frame. The dynamic equations of these four control signals can be written as [23]:

$$\frac{d}{dt} \underbrace{\begin{bmatrix} M_{Ud2} \\ M_{Ld2} \\ M_{Uq2} \\ M_{Lq2} \end{bmatrix}}_{\mathbf{x}_{ctrl}} = - \frac{d}{dt} \underbrace{\begin{bmatrix} k_{p6} I_{Ud2} \\ k_{p7} I_{Ld2} \\ k_{p8} I_{Uq2} \\ k_{p9} I_{Lq2} \end{bmatrix}}_{\mathbf{f}_{ctrl}(\mathbf{x}_{OL2})} - \underbrace{\begin{bmatrix} k_{i6} I_{Ud2} \\ k_{i7} I_{Ld2} \\ k_{i8} I_{Uq2} \\ k_{i9} I_{Lq2} \end{bmatrix}}_{\mathbf{f}_{ctrl}(\mathbf{x}_{OL2})} \quad (11)$$

It is important to note that an effective SHCSC successfully suppresses the 2nd harmonic components of the upper- and lower-arm currents in steady states. However, it is crucial to recognize that the dynamic terms of these currents still persist.

C. DC-MMC Closed-loop Nonlinear Model Without SHCSC

In this paper, the investigation reveals that the 2nd harmonic exerts a significant impact on the model accuracy, whereas the influence of 3rd and higher order harmonics is negligible. Consequently, the closed-loop model is exclusively developed for the open-loop model featuring the 2nd harmonics, as detailed in Supplementary Material A.

The DC-MMC closed-loop nonlinear model without SHCSC is obtained by combining the open-loop model (7) and the controller model (9) as:

$$\begin{cases} \dot{\mathbf{x}}_{CL2} = \mathbf{f}_{CL2}(\mathbf{x}_{CL2}, \mathbf{u}_{CL}) \\ \mathbf{x}_{CL2} = \begin{bmatrix} \mathbf{x}_{OL2} \\ \mathbf{x}_{ctrl2} \end{bmatrix}_{25 \times 1} \\ \mathbf{u}_{CL} = \begin{bmatrix} V_1 \\ V_2 \\ P_{dc,ref} \end{bmatrix} \\ \mathbf{f}_{CL2}(\mathbf{x}_{CL2}, \mathbf{u}_{CL}) = \begin{bmatrix} \mathbf{f}_{OL2}(\mathbf{x}_{OL2}, \mathbf{u}_{OL}) \\ \mathbf{f}_{ctrl}(\mathbf{x}_{OL2}, \mathbf{u}_{CL}) \end{bmatrix}_{25 \times 1} \end{cases} \quad (12)$$

The 2nd-order closed-loop nonlinear model without SHCSC has 25 states and 3 inputs.

D. DC-MMC Closed-loop Nonlinear Model with SHCSC

The DC-MMC closed-loop nonlinear model with SHCSC is obtained by combining (11) and (12) as:

$$\begin{cases} \dot{\mathbf{x}}_{CL2}^{SHCSC} = \mathbf{f}_{CL2}^{SHCSC}(\mathbf{x}_{CL2}^{SHCSC}, \mathbf{u}_{CL}) \\ \mathbf{x}_{CL2}^{SHCSC} = \begin{bmatrix} \mathbf{x}_{CL2} \\ \mathbf{x}_{ctrl2} \end{bmatrix}_{29 \times 1} \\ \mathbf{f}_{CL2}^{SHCSC} = \begin{bmatrix} \mathbf{f}_{CL2}(\mathbf{x}_{CL2}, \mathbf{u}_{CL}) \\ \mathbf{f}_{ctrl2}(\mathbf{x}_{OL2}) \end{bmatrix}_{29 \times 1} + \mathbf{U}^{SHCSC} \end{cases} \quad (13)$$

where the input vector \mathbf{U}^{SHCSC} is defined in Supplementary Material B. The 2nd-order closed-loop nonlinear model with SHCSC has 29 states and 3 inputs.

Figure 3 illustrates the block diagram of the DC-MMC closed-loop nonlinear model with SHCSC. The DC-MMC

parameters encompass the cell capacitances of the converter, arm and line inductances, and arm resistance. The model output consists of any of the 29 states or a combination. This is dependent on the input of the component that is intended to be connected to this converter.

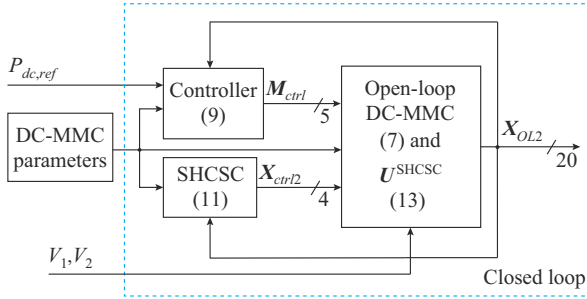


Fig. 3. Block diagram of DC-MMC closed-loop nonlinear model with SHCSC.

V. DC-MMC WITH HVDC CABLES

In this section, the inclusion of one HVDC cable on each side of the DC-MMC is contemplated to introduce dynamic behavior to the DC voltage on both sides in the event of any disturbance. This augmentation serves to enhance the study of the performance of the converter in a more realistic environment, akin to potential real-world DC systems in the future.

A. HVDC Cable Model

The HVDC cable model, as introduced in [16], is employed for the HVDC cables connected to both sides of the DC-MMC. Figure 4 presents the circuit of this model, featuring one PI section and parallel RL branches. This configuration is designed to enhance the accuracy of the HVDC cable model across a broader range of frequencies, as detailed in [16], [24], and [25].

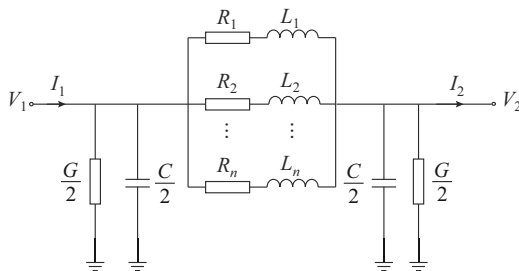


Fig. 4. Circuit of HVDC cable model.

To enhance model accuracy, incorporating multiple cascaded PI sections is advantageous, particularly for long HVDC cables, although this comes at the expense of increasing the order of both the HVDC cable and the overall system. The parallel RL values are determined using the vector fitting approach [17] while generation G and capacitance C can be derived from the cable data. The cable model can be succinctly represented in the standard state-space form provided below with the states x_{cable} be the voltages and the inductor currents of the capacitors. The output y_{cable} and inputs u_1 and u_2 can be selected as a combination of voltage and current on each

side of the HVDC cable depending on what is connected to the HVDC cable.

$$\begin{cases} \dot{x}_{cable} = A_c x_{cable} + B_c^1 u_1 + B_c^2 u_2 \\ y_{cable} = C_c x_{cable} \end{cases} \quad (14)$$

where A_c is the state matrix; B_c^1 and B_c^2 are the input matrices; and C_c is the output matrix.

B. Interconnection of DC-MMC and HVDC Cable Models

The interconnected system, composed of a DC-MMC closed-loop nonlinear model without SHCSC and two HVDC cables, is shown in Fig. 5, where V_H and V_L are the DC voltages on HV and LV sides, respectively.

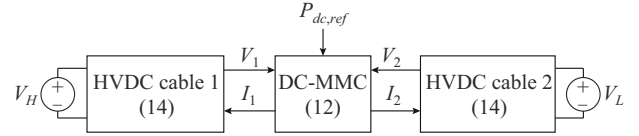


Fig. 5. Interconnected system including DC-MMC and two HVDC cables.

The interconnected system model can be given as:

$$\begin{cases} \dot{x}_{sys} = f_{sys}(x_{sys}, u_{sys}) \\ x_{sys} = \begin{bmatrix} x_{CL2} \\ x_{cable1} \\ x_{cable2} \end{bmatrix} \\ u_{sys} = \begin{bmatrix} V_H \\ V_L \\ P_{dc.ref} \end{bmatrix} \\ f_{sys} = \begin{bmatrix} f_{CL2}(x_{CL2}, u_{CL2}) \\ A_{c1} x_{cable1} + B_{c1}^1 I_1 + B_{c1}^2 V_H \\ A_{c2} x_{cable2} + B_{c2}^1 I_2 + B_{c2}^2 V_L \end{bmatrix} \end{cases} \quad (15)$$

where $I_1 = 3I_{U0}$ and $I_2 = 3(I_{U0} - I_{L0})$ are the outputs of the DC-MMC that used as the inputs to the cables. u_{CL2} can be written as:

$$u_{CL2} = \begin{bmatrix} V_1 \\ V_2 \\ P_{dc.ref} \end{bmatrix} = \begin{bmatrix} C_{c1} x_{cable1} \\ C_{c2} x_{cable2} \\ P_{dc.ref} \end{bmatrix} \quad (16)$$

VI. MODEL VERIFICATION

A. PSCAD Benchmark Model

The PSCAD benchmark model comprises a three-phase DC-MMC, as depicted in Fig. 1, connected to DC sources on both sides, either directly (Section VI-B to Section VI-E) or via HVDC cables (Section VI-F). The DC-MMC open-loop linear and closed-loop nonlinear models (7), (12), (13), and the interconnected system model (15) are implemented in MATLAB, and their accuracies are systematically evaluated against the PSCAD benchmark model.

Each DC-MMC arm valve is modelled using a type 5 model and an equivalent series resistor [26]. The key parameters of the DC-MMC are outlined in Table I. The internal operating frequency of the converter, as a crucial design parameter influencing size and power loss [21], is set to be

150 Hz in this paper.

TABLE I
DC-MMC PARAMETERS

Parameter	Value	Parameter	Value
P_{rated} (MW)	600	R_{armU} (Ω)	1.44
V_H (kV)	320	R_{armL} (Ω)	0.96
V_L (kV)	250	V_{U0ref}^{Σ} (kV)	320
N_U, N_L	160, 160	V_{L0ref}^{Σ} (kV)	320
C_{SMU} (mF)	4.4	L_{arm} (mH)	11
C_{SML} (mF)	12.2	L_2 (mH)	80

B. Verification of DC-MMC Open-loop Linear Model

The accuracy of the DC-MMC open-loop linear model (7) is validated against the PSCAD benchmark model under various disturbances. For brevity, only the results depicting the upper-arm current in response to a 5% step-down on the LV side voltage are presented, as shown in Fig. 6. The control modulation indices for this test case are: $M_{U0}=0.217$, $M_{L0}=0.777$, $M_U=0.217$, $M_{Ld}=0.219$, and $M_{Lq}=0.042$.

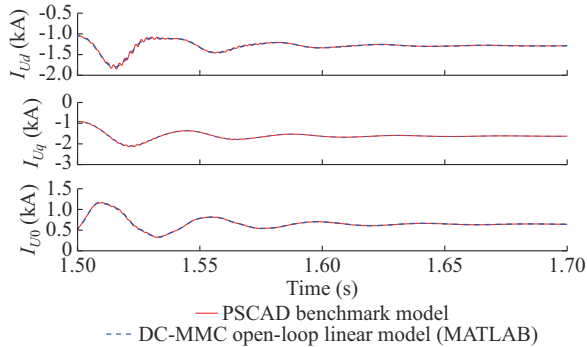


Fig. 6. Results for upper-arm current in response to 5% step-down on LV side voltage.

The observed good matching indicates that the proposed DC-MMC open-loop linear model is highly accurate.

C. Impact of 2nd and 3rd Harmonics on Model Accuracy

The study examines the influence of the 2nd and 3rd harmonics on model accuracy. To conduct this investigation, two additional models are developed: ① a 1st-order model comprising only zero sequence and fundamental frequency, and ② a 3rd-order model encompassing zero sequence, fundamental frequency, and 2nd and 3rd harmonics. The respective orders of the 1st-, 2nd-, and 3rd-order open-loop models are 12, 20, and 28, respectively.

The model accuracy is validated against the PSCAD benchmark model, and the errors of the upper-arm current for a 5% step-down on the LV side voltage at $t=1.5$ s are depicted, as shown in Fig. 7, where $I_{U0,err}$, $I_{Uq,err}$, and $I_{Ud,err}$ refer to the errors of I_{U0} , I_{Uq} , and I_{Ud} , respectively. Notably, the error of the 1st-order open-loop model is considerably higher than those of the other two models, while the errors of the 2nd- and 3rd-order open-loop models are very small

and nearly identical. This suggests that the impact of the 2nd harmonics on model accuracy is significant and should be considered in many applications. Conversely, the 3rd harmonics (and higher harmonics) have a negligible impact and can be safely ignored. Consequently, the 2nd-order open-loop model, which includes zero sequence, fundamental frequency, and 2nd harmonics, is adopted in this paper.

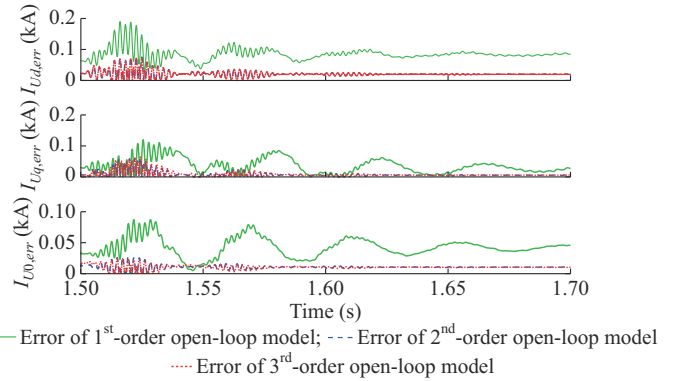


Fig. 7. Impact of 2nd and 3rd harmonics on model accuracy.

D. Verification of DC-MMC Closed-loop Nonlinear Model

The accuracy of the DC-MMC closed-loop nonlinear model (12) is validated against the PSCAD benchmark model under various step inputs. Figure 8 illustrates the results for the upper-arm sum voltage in response to a 5% step-up on the HV side voltage at $t=1.5$ s. The good matching observed in the results verifies that the proposed DC-MMC closed-loop nonlinear model is highly accurate.

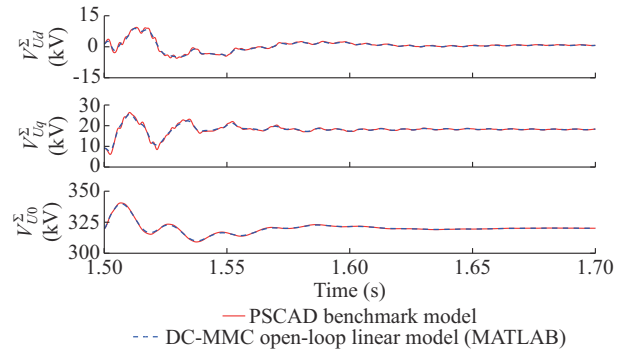


Fig. 8. Results for upper-arm sum voltage in response to a 5% step-up on HV side voltage.

E. Impact of SHCSC on Accuracy of DC-MMC Closed-loop Nonlinear Model

This subsection examines the impact of SHCSC on the accuracy of the DC-MMC closed-loop nonlinear model. In Fig. 9, the results illustrate the response of the upper-arm voltage $V_{armU}(t) = m_U(t)V_U^{\Sigma}(t)$ to a 5% step-up on the HV side voltage. It is observed that the DC-MMC closed-loop nonlinear model with SHCSC (13) demonstrates an insignificant improvement compared with the DC-MMC closed-loop nonlinear model without SHCSC (12). Nevertheless, considering the adequate accuracy and lower-order of the DC-MMC closed-loop nonlinear model without SHCSC, it is employed

in the subsequent section to assess the impact of HVDC cable on the DC-MMC.

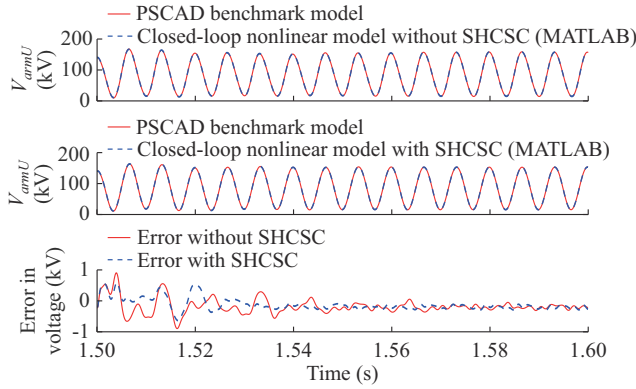


Fig. 9. Results for upper-arm voltage in response to a 5% step-down on HV side voltage.

F. Verification of Interconnected System Model

The proposed interconnected system (15) integrates one DC-MMC and two 100 km HVDC cables. Initially, the HVDC cable model is developed using a single PI section with multiple parallel RL branches, as shown in Fig. 4. The accuracy of the HVDC cable model is verified against a wide-band cable model (PSCAD) across a frequency spectrum ranging from 0.001 Hz to 5000 Hz. Figure 10 shows the magnitude and phase of 100 km HVDC cable models with 3, 5, and 7 parallel RL branches against wide-band cable model. It is observed that the HVDC cable model utilizing 5 parallel RL branches achieves a high degree of accuracy. A higher-order cable model, either with additional PI sections or more parallel RL branches, slightly improves the accuracy but also increases the order and complexity of the model.

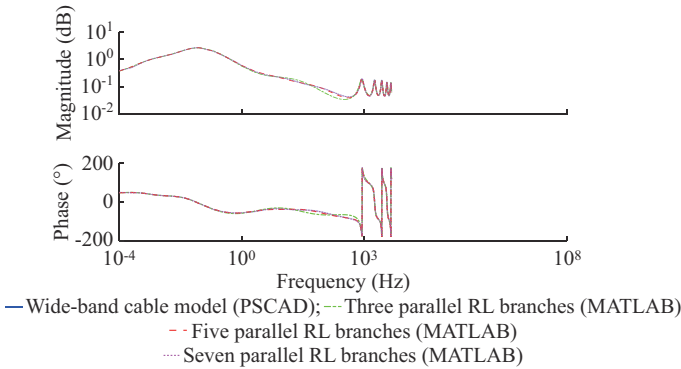


Fig. 10. Magnitude and phase of 100 km HVDC cable models with 3, 5, and 7 parallel RL branches against wide-band cable model.

Figure 11 illustrates the results for the lower-arm sum voltage in response to a 5% step-up on the HV side voltage at $t=1.5$ s. The observed good matching indicates that the proposed model is accurate and well-suited for design and analysis purposes.

Figure 12 shows the impact of cable length on DC-MMC DC voltage dynamic in response to a 5% step-up on LV side voltage. The introduction of HVDC cables imparts dynamics to the DC voltages on both sides of the DC-MMC. The

lengthening of HVDC cables amplifies this dynamic effect, potentially leading to system instability, a topic that will be explored in the subsequent section.

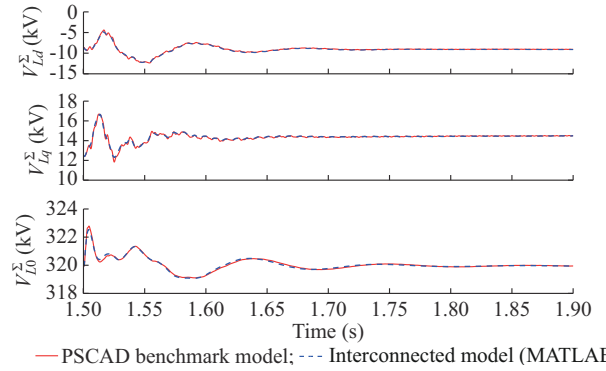


Fig. 11. Results for lower-arm sum voltage in response to a 5% step-up on HV side voltage (DCMMC+two 100 km cables).

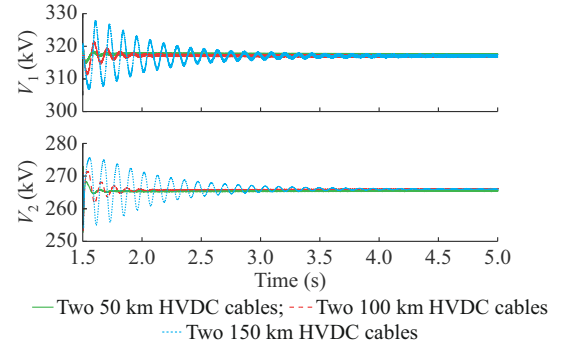


Fig. 12. Impact of cable length on DC-MMC DC voltage dynamic in response to a 5% step-up on LV side voltage.

VII. STABILITY ANALYSIS AND DAMPING CONTROL DESIGN

The proposed interconnected system models are versatile tools applicable for stability analysis and controller design. In this section, the interconnected system model is employed to conduct a thorough analysis of system stability. Subsequently, a damping controller is designed to mitigate oscillations and stabilize the system.

A. Impact of Cable Length on Interconnected System Stability

Table II provides the most sensitive eigenvalues of the interconnected system for varying cable lengths. As observed, the eigenvalues shift towards the right half-plane with increasing cable length, indicating a growing oscillatory tendency. Notably, the interconnected system reaches instability for HVDC cables longer than 190 km.

TABLE II
MOST SENSITIVE EIGENVALUES OF INTERCONNECTED SYSTEM FOR VARYING CABLE LENGTH

Cable length (km)	Most sensitive eigenvalue
50	$-20.35 \pm 69.46i$
100	$-13.15 \pm 69.84i$
150	$-5.95 \pm 65.21i$
190	$0.0046 \pm 61.42i$

B. Damping Control Design

The stability analysis of the interconnected system reveals that the generic control structure illustrated in Fig. 2 is insufficient for effectively damping oscillations and stabilizing the system. Consequently, the introduction of a suitable damping controller becomes imperative.

The damping controller is designed to monitor one or more states within the interconnected system and adjust one of the outputs of the generic controller presented in Fig. 2. To identify the optimal states for feedback, the approach is employed [27]. PFs are computed by element-wise multiplication of the right and left eigenvectors associated with the matrix A of the linearized system in (15).

These PFs are calculated and normalized across various cable lengths, and the states with the highest PF are selected as the most suitable candidates for the feedback signals [18]. As an example, in a system with 100 km cable length, the highest PF is 0.192, corresponding to the 2nd harmonic components of V_{Ud2}^{Σ} and V_{Uq2}^{Σ} .

To determine the best control inputs to pair with the selected feedback signals V_{Ud2}^{Σ} or V_{Uq2}^{Σ} , the residue approach is employed [20]. In Table III, the calculated residue values are presented for the 5 generic control signals to pair with V_{Ud2}^{Σ} or V_{Uq2}^{Σ} for the interconnected system with 100 km cable length. The pair $(\phi_{m_i}, V_{Ud2}^{\Sigma})$ exhibits the highest magnitude and is thus selected for the damping control.

TABLE III
RESIDUE VALUES OF SELECTED FEEDBACK SIGNALS AND
GENERIC CONTROL SIGNALS

Generic control signal	Residue value	
	V_{Ud2}^{Σ}	V_{Uq2}^{Σ}
I_{Uref}	2.140	2.140
I_{Lref}	0.005	0.005
M_{U0}	0.016	0.016
M_{L0}	0.010	0.010
ϕ_{m_i}	2.150	2.140

Figure 13 depicts the revised control block diagram with the integrated damping controller. The signal V_{Ud2}^{Σ} is filtered and added, with gain K_{damp} , to the control signal ϕ_{m_i} . The band pass filter (BPF) has a resonant frequency of 4 Hz and a damping ratio of 0.707, where the resonant frequency is determined based on the oscillation frequency of V_{Ud2}^{Σ} after applying a step disturbance. Notably, after applying this disturbance step, an oscillation frequency between 3.5 Hz and 7 Hz becomes apparent in V_{Ud2}^{Σ} without the damping controller. Subsequent fine-tuning reveals that a resonant frequency of 4 Hz significantly enhances system performance. Here, the damping gain $K_{damp} = -0.15$ is selected.

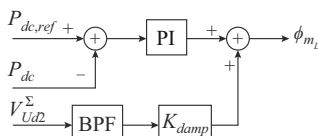


Fig. 13. Revised control block diagram with integrated damping controller.

C. Verification of Damping Controller

The effect of the damping controller on the performance of the interconnected system is scrutinized for varying cable lengths. Table IV provides the most sensitive eigenvalues of the interconnected system for different cable lengths, both with and without the damping controller. Notably, the proposed damping controller induces a shift of the eigenvalues towards the left, indicative of a more stable system. Remarkably, the proposed damping controller demonstrates the capability to stabilize the system for HVDC cables with up to 337 km cable length.

TABLE IV
MOST SENSITIVE EIGENVALUES OF INTERCONNECTED SYSTEM FOR
DIFFERENT CABLE LENGTHS WITH AND WITHOUT DAMPING CONTROLLER

Cable length (km)	Most sensitive eigenvalue without damping controller	Most sensitive eigenvalue with damping controller
50	$-20.35 \pm 69.46i$	$-28.83 \pm 51.92i$
100	$-13.15 \pm 69.84i$	$-26.97 \pm 49.94i$
150	$-5.95 \pm 65.21i$	$-10.71 \pm 59.55i$
190	$0.0046 \pm 61.42i$	$-2.90 \pm 59.62i$
250	$5.64 \pm 56.74i$	$-1.63 \pm 61.47i$
300	$8.80 \pm 53.02i$	$-0.32 \pm 55.18i$
337	$10.28 \pm 50.01i$	$0.0017 \pm 55.19i$

Figure 14 shows the upper-arm sum voltage results for a 5% step-up on LV side voltage with and without the damping controller while the cable length is 100 km. It is evident that the damping controller significantly diminishes the oscillations. In Fig. 15, the results are represented with the cable length extended to 190 km. Notably, the system exhibits instability without the damping controller, but the stability is restored by including the damping controller. The simulation results are consistent with the eigenvalue analysis given in Table IV.

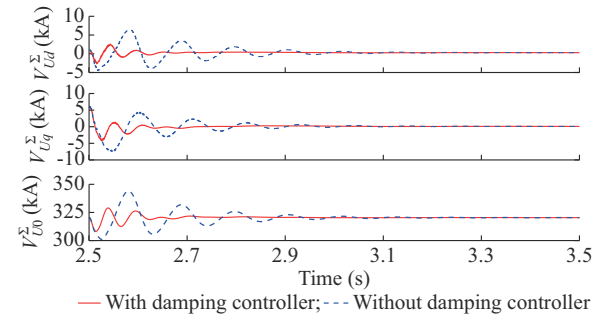


Fig. 14. Results for upper-arm sum voltage in response to 5% step-up on LV side voltage with and without damping controller.

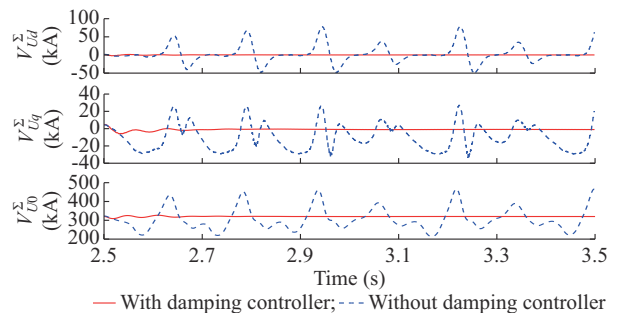


Fig. 15. Results for upper-arm sum voltage in response to 5% step-up on LV side voltage with 190 km cable lengths.

VIII. CONCLUSION

This paper presents a robust and comprehensive modeling approach for DC-MMC systems, introducing a 20th-order open-loop linear model and a 25th-order closed-loop nonlinear model. These models meticulously account for converter variables across three dq frames, effectively addressing significant coupling effects. Validation against PSCAD benchmark models demonstrates the high accuracy of the proposed model.

A critical investigation into the impact of harmonics reveals that while the 2nd harmonic notably affects the model accuracy, higher order harmonics are largely negligible, streamlining the analysis process. Efforts to enhance the DC-MMC closed-loop nonlinear model through the integration of SHCSC model provide limited improvements, reinforcing the robustness of the original model structure. Expanding the application of the model, the DC-MMC closed-loop nonlinear model is integrated with two HVDC cables modeled using the vector fitting approach, creating an interconnected system model. This advanced interconnected system model enables a detailed analysis of the influence of cable length on system performance. To ensure stability in the interconnected systems with extended cable lengths, a damping controller is successfully designed and implemented. The insights gained here provide valuable guidance for practical implementation of interconnected systems, particularly in enhancing system stability under varying cable lengths.

REFERENCES

- [1] G. J. Kish, M. Ranjram, and P. W. Lehn, "A modular multilevel DC/DC converter with fault blocking capability for HVDC interconnects," *IEEE Transactions on Power Electronics*, vol. 30, no. 1, pp. 148-162, Jan. 2015.
- [2] D. Jovcic, P. Dworakowski, G. J. Kish *et al.*, "Case study of non-isolated MMC DC-DC converter in HVDC grids," in *Proceedings of CI-GRE Symposium*, Aalborg, Denmark, Jun. 2019, pp. 1-8.
- [3] D. Jovcic, *High Voltage Direct Current Transmission: Converters, Systems and DC Grids*, New York: Wiley, 2019.
- [4] R. Razani and Y. A.-R. I. Mohamed, "Operation limits of the hybrid DC/DC modular multilevel converter for HVDC grids connections," *IEEE Journal of Emerging and Selected Topics in Power Electronics*, vol. 9, pp. 4459-4469, Sept. 2021.
- [5] D. Jovcic, "Rotating frame, average value converter modeling," *IEEE Electrification Magazine*, vol. 11, pp. 20-28, Jan. 2023.
- [6] *HVDC Grid Feasibility Study*, CIGRE WG B4.52, 2013.
- [7] *Control Methodologies for Direct Voltage and Power Flow in Meshed HVDC Grid*, CIGRE WG B4.58, 2017.
- [8] *DC-DC Converters in HVDC Grids and for Connections to HVDC Systems*, CIGRE WG B4.76, 2021.
- [9] S. Engel, M. Stieneker, N. Soltan *et al.*, "Comparison of the modular multilevel DC converter and the dual-active bridge converter for power conversion in HVDC and MVDC grids," *IEEE Transactions on Power Electronics*, vol. 30, no. 1, pp. 124-137, Jan. 2015.
- [10] H. Yang, J. Qin, S. Debnath *et al.*, "Phasor domain steady-state modeling and design of the DC-DC modular multilevel converter," *IEEE Transactions on Power Delivery*, vol. 31, no. 5, pp. 2054-2063, Oct. 2016.
- [11] H. Yang, M. Saeedifard, and A. Yazdani, "An enhanced closed-loop control strategy with capacitor voltage elevation for the DC-DC MMC," *IEEE Transactions on Industrial Electronics*, vol. 66, no. 3, pp. 2366-2375, Mar. 2019.
- [12] G. J. Kish and P. W. Lehn, "Linearized DC-MMC models for control design accounting for multifrequency power transfer mechanisms," *IEEE Transactions on Power Delivery*, vol. 33, no. 1, pp. 271-281, Feb. 2018.
- [13] A. Jamshidifar and D. Jovcic, "Phasor analytical model of non-isolated DC/DC converter based on modular multilevel converter for DC transmission grid," *Journal of Modern Power System and Clean Energy*, vol. 11, no. 2, pp. 611-621, Mar. 2023.
- [14] R. Razani and Y. A.-R. I. Mohamed, "Analysis of the unsymmetrical operation of the DC/DC MMC considering the DC-link impedance," *IEEE Transactions on Power Delivery*, vol. 37, no. 3, pp. 1723-1733, Mar. 2022.
- [15] S. D'Arco, J. A. Suul, and J. Beerten, "Configuration and model order selection of frequency-dependent π models for representing DC cables in small-signal eigenvalue analysis of HVDC transmission systems," *IEEE Journal of Emerging and Selected Topics in Power Electronics*, vol. 9, pp. 2410-2426, Aug. 2021.
- [16] S. Kovacevic, D. Jovcic, P. Rault *et al.*, "Small signal state space model of the frequency-dependent DC cable based on direct vector fitting," in *Proceedings of 15th IET International Conference on AC and DC Power Transmission (ACDC 2019)*, Coventry, UK, Aug. 2019, pp. 1-8.
- [17] B. Gustavsen and A. Semlyen, "Rational approximation of frequency domain responses by vector fitting," *IEEE Transactions on Power Delivery*, vol. 14, no. 3, pp. 1052-1061, Jul. 1999.
- [18] W. Lin, D. Jovcic, and S. M. Fazeli, "Distributed power balance and damping control for high power multiport LCL DC hub," *Electric Power Systems Research*, vol. 129, pp. 185-193, Sept. 2015.
- [19] S. Skogestad and I. Postlethwaite, *Multi Variable Feedback Control Analysis and Design*, New York: John Wiley & Sons, 2004.
- [20] N. Yang, Q. Liu, and J. McCalley, "TCSC controller design for damping interarea oscillations," *IEEE Transactions on Power Systems*, vol. 13, no. 4, pp. 1304-1310, Apr. 1998.
- [21] A. Jamshidifar, D. Jovcic, A. Nami *et al.* (2021, Jan.). Selecting frequency and parameters of DC-fault tolerant non-isolated high power MMC DC/DC converter. [Online]. Available: <https://doi.org/10.1016/j.epr.2020.106896>
- [22] S. Badkubi, A. Jamshidifar, and S. Aphale, "Dynamic DQ model of DC-modular multilevel converter for DC grid applications," in *Proceedings of IEEE Conference on Power Electronics and Renewable Energy (CPERE)*, Luxor, Egypt, Feb. 2023, pp. 1-6.
- [23] A. Jamshidifar and D. Jovcic, "Small-signal dynamic DQ model of modular multilevel converter for system studies," *IEEE Transactions on Power Delivery*, vol. 31, no. 1, pp. 191-199, Jan. 2016.
- [24] J. R. Macías, A. Gómez-Expósito, and A. B. Soler, "A comparison of techniques for state-space transient analysis of transmission lines," *IEEE Transactions on Power Delivery*, vol. 20, no. 2, pp. 894-903, Apr. 2005.
- [25] J. Beerten, S. D'Arco, and J. A. Suul, "Frequency-dependent cable modelling for small-signal stability analysis of VSC-HVDC systems," *IET Generation, Transmission, and Distribution*, vol. 10, no. 6, pp. 1370-1381, Jul. 2016.
- [26] H. Zhang, D. Jovcic, W. Lin *et al.*, "Average value MMC model with accurate blocked state and cell charging/discharging dynamics," in *Proceedings of 2016 4th International Symposium on Environmental Friendly Energies and Applications (EFEA)*, Belgrade, Serbia, Sept. 2016, pp. 1-8.
- [27] P. Kundur and M. P. Om, *Power System Stability and Control*. Toronto: McGraw-Hill, 2022.

Salman Badkubi received the B.S. degree from Isfahan University of Technology, Isfahan, Iran, in 2008, and the M.S. degree from Urmia University, Urmia, Iran, in 2011. He is currently pursuing the Ph.D. degree at the University of Aberdeen, Aberdeen, UK. His research interests include power electronics, high-voltage direct current, power system analysis, and renewable energy.

Aliakbar Jamshidi Far received the B.Sc., M.Sc., and Ph.D. degrees all in electrical engineering from Sharif University of Technology, Tehran, Iran, in 1992, Iran University of Science and Technology, Tehran, Iran, in 1996, and Amirkabir University of Technology, Tehran, Iran, in 2008. From 2008 to 2012, he was an Assistant Professor with Iranian Research Organization for Science and Technology, Tehran, Iran. He joined the University of Aberdeen, Aberdeen, UK, in 2012, as a Research Fellow, and is currently a Lecturer with the School of Engineering, University of Aberdeen. His research interests include high-voltage direct current, renewable energy, and control system.

Sumeet S. Aphale is the Director of the Artificial Intelligence, Robotics and Mechatronic Systems Group (ARMS), at the School of Engineering, University of Aberdeen, Aberdeen, UK. His research has been published in over

120 peer-reviewed journals and conferences and has won several Best Paper Awards and nominations. He has served as an Associate Editor for IEEE Control systems Magazine, IEEE Control Systems Society's Conference Editorial Board, Frontiers of Mechanical Engineering (Mechatronics) and,

Shock and Vibration. With career spanning over two decades, his research interests include design, analysis, and control of robotic and mechatronic systems, subsea actuators, biomedical device, renewable energy solution, as well as sensing and precision actuation technology.